Article

Zinc Storage Performance of Oxygen-Deficient NH$_4$V$_3$O$_8$: Theoretical and Experimental Study

He Lin *, Xuanxuan Cai and Yu Zhang

A State Key Laboratory of Chemistry and Utilization of Carbon Based Energy Resources, School of Chemistry, Xinjiang University, Urumqi 830017, China; xiaow1456@gmail.com (X.C.); cnuo017@gmail.com (Y.Z.)
* Correspondence: helin@xju.edu.cn; Tel.: +86-180-4090-9207

Abstract: Using density functional theory (DFT), the density of states of NH$_4$V$_3$O$_8$ (NVO) was analyzed pre- and post-oxygen defect (O$_d$) formation. The findings revealed a reduced bandgap in NVO after O$_d$ introduction, emphasizing the role of O$_d$ in enhancing conductivity of the material, thus improving its electrochemical attributes. Through the water bath method, both NVO and its oxygen-deficient counterpart, (NH$_4$)$_2$V$_{10}$O$_{25}$·8H$_2$O (NVO$_d$), were synthesized as potential cathode materials for aqueous zinc-ion batteries (AZIBs). Experimental outcomes resonated with DFT predictions, highlighting the beneficial role of oxygen defects in boosting electrical conductivity. Notably, the refined material displayed a remarkable capacity of 479.3 mAh g^{-1} at 0.1 A g^{-1}, underscoring its promise for advanced energy storage solutions.

Keywords: oxygen defects; density functional theory; aqueous zinc-ion batteries; vanadium oxides

1. Introduction

The escalating energy crisis, exacerbated by a notable scarcity of resources, has catalyzed the advances in electrochemical energy storage devices. This surge in development is in direct response to the burgeoning demand for diverse sources of renewable and clean energy [1]. A paramount challenge presented by these renewable energy sources is their intrinsic intermittency, which underscores the critical need for efficient energy storage solutions in the lexicon of modern scientific inquiry. In the last decade, lithium-ion batteries (LIBs) have ascended to prominence within this sphere, drawing considerable interest due to their superior energy density and impressive life cycle. Such characteristics have cemented their position as a cornerstone in the field of electrochemical energy storage [2]. Nonetheless, the limited availability of lithium, rising costs, and potential safety hazards associated with the use of organic electrolytes have raised significant concerns [3,4]. This has sparked an increasing interest among the scientific community in investigating alternative battery technologies that promise greater ecological sustainability, cost efficiency, and inherent safety.

In the realm of battery technologies, aqueous zinc-ion batteries (AZIBs) have garnered attention as a promising alternative. Their increasing significance is attributed to a constellation of favorable characteristics, including the abundant availability of zinc resources worldwide, the environmentally friendly nature of zinc utilization, an impressive theoretical specific capacity of 820 mAh g^{-1}, and a beneficial redox potential of -0.76 V versus the standard hydrogen electrode (SHE) [5]. Within this context, the cathode material plays a critical role in defining the electrochemical performance of AZIBs. To date, a wide range of cathode materials capable of accommodating Zn^{2+} ions have been investigated. These include manganese oxides (e.g., MnO$_2$, Mn$_2$O$_3$, Mn$_3$O$_4$) [6–11], vanadium oxides (e.g., VO$_2$, V$_2$O$_5$, Na$_2$V$_6$O$_{16}$·1.63H$_2$O) [12–15], Prussian blue analogs (e.g., Zn$_3$[Fe(CN)$_6$]$_2$) [16–18], and a variety of emerging materials [19–23].

Vanadium-based materials, distinguished by their versatile valence states and open-framework structures, have emerged as frontrunners for application as cathodes in AZIBs.

Their superior zinc storage capacities and remarkable cyclability position them as compelling candidates in the quest for high-performance energy storage solutions [24,25]. Despite these advantages, a critical bottleneck in the deployment of these materials is the electrostatic attraction between Zn^{2+} ions and vanadium oxide layers. This interaction significantly hampers the mobility of Zn^{2+} ions within the layered structures, posing a challenge to achieving optimal battery performance.

The recent strategies aimed at overcoming this challenge include electrostatic shielding and the expansion of ion diffusion pathways, which have shown promising results in facilitating Zn^{2+} ion migration [26]. Notably, approaches such as doping with interlayer metal ions (e.g., $Na_{0.33}V_2O_5$, $Li_{0.7}V_6O_{15}$) and incorporating structural water ($V_2O_5 \cdot nH_2O$) have been adopted to enhance the structural dynamics of these materials. However, while these methods improve ion diffusion channels, the contribution of the introduced heavier metal ions to Zn^{2+} storage remains marginal [27].

In contrast, the use of $NH_4V_3O_8$ (NVO) nano-belts represents a novel direction. These nano-belts utilize lighter NH_4^+ ions as structural pillars, not only facilitating the expansion of diffusion pathways but also significantly boosting the volumetric and gravimetric energy capacities for AZIB cathodes. The formation of hydrogen bonds between NH_4^+ ions and VO layers introduces additional cohesion within the layered structure, enhancing its structural stability and integrity [28–30]. Furthermore, our study explores the strategic introduction of defects, such as oxygen vacancies, into the crystal lattice. This approach is posited as a groundbreaking means of elevating AZIB performance, promoting enhanced ion diffusion kinetics, more efficient ion intercalation and deintercalation, while concurrently averting undesired phase transitions and tailoring the material's conductivity [31].

Our research fills a critical gap in the existing literature by offering a comprehensive understanding of how NH_4^+ ion incorporation and intentional defect engineering can synergistically improve the functionality of vanadium-based cathodes in AZIBs. Initially, density functional theory (DFT) calculations were employed to investigate the alterations in the density of states for NVO consequent to the induction of oxygen defects (O_ds). The findings from these calculations revealed a reduction in the bandgap of NVO subsequent to the integration of O_ds. This observation suggests that the presence of O_ds within the VO layers modulates the material's internal structure, thereby augmenting its electrical conductivity—a factor that is pivotal for the amelioration of electrochemical performance.

Subsequently, employing a water bath synthesis method, NVO and oxygen-deficient $(NH_4)_2V_{10}O_{25} \cdot 8H_2O$ (NVO_d) nanosheets were synthesized and evaluated as cathode materials for AZIBs. The congruence between experimental outcomes and theoretical predictions underscores the efficacy of oxygen defects in bolstering the electrical conductivity of the crystal structure. The NVO_d material demonstrated an exemplary capacity, achieving 479.3 mAh g^{-1} at a current density of 0.1 A g^{-1}. This evidence firmly establishes the significant role of O_ds in enhancing the electrochemical attributes of vanadium-based cathode materials for AZIB applications.

2. Results and Discussion

2.1. DFT Calculations

Layered cathode materials are poised to play a pivotal role in the advancement of AZIBs, attributed to their inherent potential for high energy storage capacities. However, the practical application of these materials is significantly hindered by the sluggish diffusion kinetics of Zn^{2+}, a phenomenon often precipitated by the structural collapse of the cathode material during electrochemical cycling. In an effort to circumvent this challenge, the strategic integration of O_ds within the vanadium oxide (VO) layers has been identified as a promising approach to reinforce structural stability and enhance Zn^{2+} diffusion kinetics.

To rigorously evaluate the impact of O_d incorporation on the structural and electrochemical performance of NVO cathodes, DFT calculations were undertaken. These computational analyses aimed to elucidate the variations in electronic structure of NVO

before and after the introduction of O_ds, and further assess how these oxygen vacancies alter the electronic density of states.

Figure 1a–c delineates the schematic representations of the conventional cell structures for three distinct configurations: the pristine NVO structure, NVO-O_d, and the configuration of NVO-O_d subsequent to the incorporation of Zn^{2+} ions (Zn-NVO$_d$). Initially, to ascertain the impact of O_ds on the electrical conductivity of these systems, density of states (DOS) calculations were performed. The DOS analysis, illustrated in Figure 1d, reveals that the band gap of pristine NVO is quantified at 1.49 eV. Upon the introduction of O_ds, there is a significant reduction in the band gap to 0.185 eV, highlighting the enhanced metallic character of NVO-O_d which is indicative of improved conductivity. This enhancement in conductivity is attributed to the structural modifications induced by the incorporation of O_ds into the NVO matrix, which not only facilitates the insertion and extraction of Zn^{2+} ions but also provides additional electrons to augment the capacity.
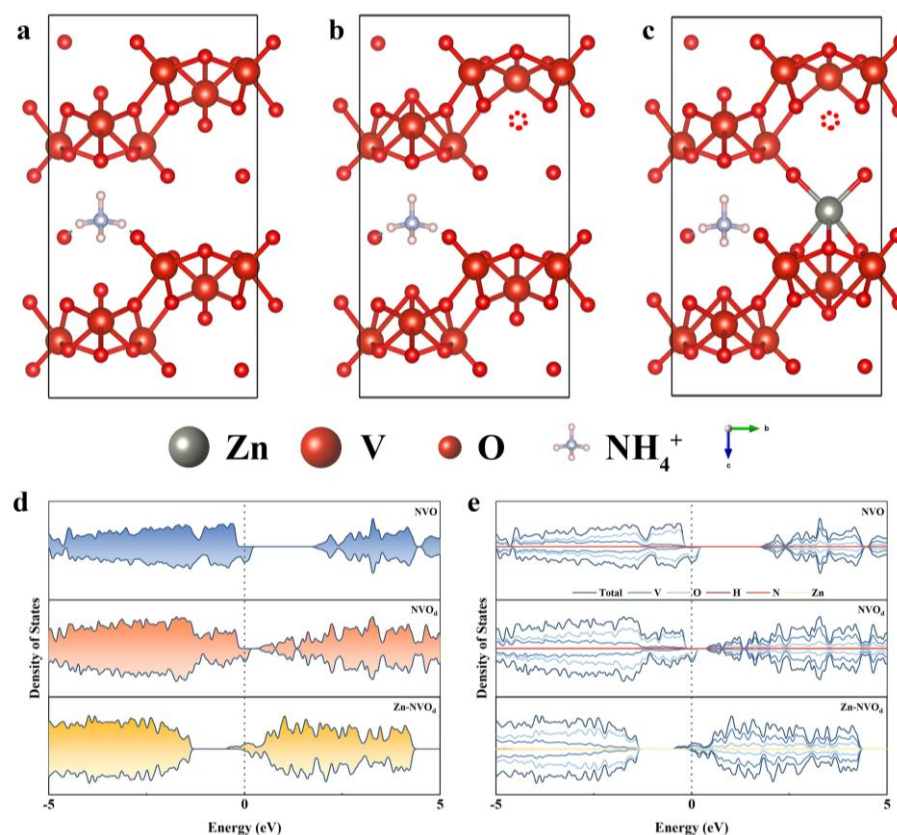

Figure 1. Conventional unit cell of (**a**) NVO, (**b**) NVO$_d$, and (**c**) Zn-NVO$_d$ after Zn^{2+} insertion; (**d**) DOS and (**e**) PDOS of the above three structures.

Subsequent to the embedding of Zn^{2+} into NVO-O_d, the band gap is observed to vanish, with the emergence of a new peak at the Fermi level, as depicted in Figure 1e. The projected density of states (PDOSs) analysis for the three systems elucidates distinct variations in the state density distributions, particularly around the Fermi level. Notably, the incorporation of Zn^{2+} into NVO-O_d results in the Fermi level being shifted below 0 eV, with discernible states associated with vanadium (V) evident at the Fermi level. The introduction of O_ds into the NVO framework notably influences electron transfer processes related to V; the embedding of Zn^{2+} ions transforms the material's character to metallic, thereby enhancing electron mobility within the material. This series of observations underscores the critical role of O_ds in modulating the electronic structure and optimizing the electrochemical performance of NVO-based cathodes for aqueous zinc-ion batteries.

2.2. Composition and Structural Characterization

Utilizing the reductive capabilities of thiourea in acidic environments, nanosheets of oxygen-deficient NVO_d were synthesized via a straightforward water bath methodology, employing NH_4VO_3 as the starting material. The decomposition of thiourea under heated acidic conditions results in the generation of ammonia, carbon dioxide, and hydrogen sulfide (H_2S) gas through a hydrolysis reaction. The evolution of H_2S gas during this process facilitates the introduction of O_ds into the forming NVO_d, acting as Lewis acid sites. To explore the effect of varying thiourea concentrations, different molar quantities of thiourea (2, 3, and 4 mmol) were utilized, resulting in the synthesis of distinct batches of NVO_d, designated as NVO_d-2 (with 2 mmol thiourea), NVO_d-3 (with 3 mmol thiourea), and NVO_d-4 (with 4 mmol thiourea). For comparative purposes, a control batch of NVO material was also prepared under identical conditions but without the addition of thiourea.

The crystalline structure of the synthesized $(NH_4)_2V_{10}O_{25}\cdot8H_2O$ was characterized using X-ray diffraction (XRD) analysis. The XRD patterns for the derived NVO_d and $NH_4V_3O_8$ specimens are presented in Figure 2a. Analysis revealed that the diffraction peaks corresponding to NVO_d-2, NVO_d-3, and NVO_d-4 samples align with the (001), (003), (004), (020), and (420) planes, as per the standard powder diffraction file (PDF) card for $(NH_4)_2V_{10}O_{25}\cdot8H_2O$ (JCPDS number: 26-0097), indicating a pure phase of NVO_d with no detectable impurities resulting from the thiourea addition.
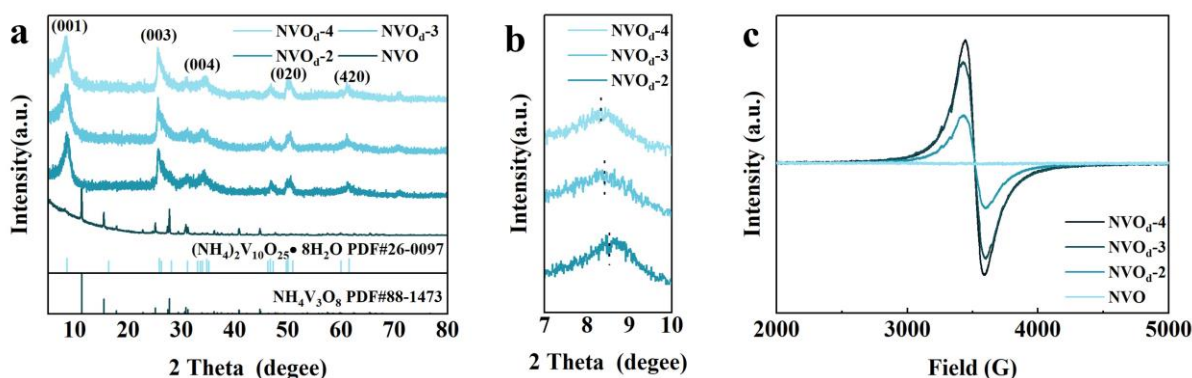

Figure 2. (**a**) XRD patterns of NVO_d-2, NVO_d-3, NVO_d-4, and NVO; (**b**) partial XRD patterns of NVO_d; (**c**) EPR spectroscopy of NVO_d-2, NVO_d-3, NVO_d-4, and NVO.

The transformation from $NH_4V_3O_8$ to $(NH_4)_2V_{10}O_{25}$ represents a critical phase in the synthesis process of NVO_d materials, characterized by a complex interplay of structural and electronic modifications. This transition is fundamentally driven by the extraction of oxygen atoms from the lattice of $NH_4V_3O_8$, resulting in the emergence of defect sites enriched with excess electrons. These surplus electrons play a significant role in augmenting the delocalized electron cloud, particularly increasing the electron density in proximity to vanadium (V) sites. Such an enhancement in electron density around V atoms triggers a reorganization of VO structural units, eventually leading to the formation of the $(NH_4)_2V_{10}O_{25}$ structure. This reorganization is not merely a rearrangement but is accompanied by the reduction of V atoms from a higher to a lower oxidation state. The creation of oxygen vacancies plays a pivotal role in this process, as it directly contributes to the increased electron density around the V atoms, facilitating their reduction. Consequently, this leads to the stabilization of the $(NH_4)_2V_{10}O_{25}$ structure.

In addition, a detailed examination of the XRD spectra, particularly around the (001) diffraction peak, is illustrated in Figure 2b. The observed shift of the (001) diffraction peak towards lower angles with an increase in thiourea concentration suggests an expansion in the interlayer spacing of the material. This phenomenon indicates that the introduction of O_d via thiourea not only modifies the internal crystal structure but also induces a structural rearrangement that impacts the interlayer distance, facilitating enhanced electrochemical functionality.

Electron paramagnetic resonance (EPR) spectroscopy was utilized to ascertain the presence of O_ds within the synthesized materials, as depicted in Figure 2c. The distinct sharp signal observed in the EPR spectrum of NVO_d can be attributed to electrons localized at defect sites, with the resonance corresponding to a g-value of approximately 2.02, indicative of O_ds. Notably, the intensity of this signal—and hence the concentration of oxygen vacancies—shows a direct correlation with the quantity of thiourea used during the synthesis process. In stark contrast, samples of NVO prepared in the absence of thiourea exhibited no discernible Lorentzian EPR signals, unequivocally indicating a lack of detectable O_ds within these materials. This observation underscores the pivotal role of thiourea as a facilitator of structural transformation, specifically through the induction of oxygen vacancies. Such vacancies are instrumental in modifying the electronic structure and enhancing the functional properties of the material, as evidenced by the pronounced EPR signals in thiourea-treated samples. This finding corroborates the hypothesis that thiourea not only acts as a reducing agent but also as a structural modifier, introducing beneficial defects that can significantly influence the material's electrochemical performance.

The surface morphology of the synthesized materials was meticulously examined using scanning electron microscopy (SEM). The SEM images, as presented in Figure 3a–i, illustrate the NVO_d samples with varying degrees of oxygen deficiency (NVO_d-2, NVO_d-3, and NVO_d-4) at multiple magnifications. These depictions reveal that the NVO_d samples consist of nanosheets with irregular shapes, predominantly featuring thicknesses within the 70 to 90 nm range. Notably, a morphological evolution is observed as the oxygen deficiency level increases; the samples exhibit a transition from voluminous to more fragmented nanosheets, while the thickness of these structures remains relatively constant across the variants.

To further elucidate the compositional homogeneity of the synthesized NVO_d nanosheets, energy-dispersive X-ray spectroscopy (EDS) mapping analysis was conducted. The EDS results, illustrated in Figure 3j, confirm the uniform distribution of nitrogen (N), oxygen (O), and V elements across the nanosheets. Notably, sulfur (S) was not detected in the EDS analysis, indicating the effective incorporation of oxygen defects without introducing sulfur impurities into the material. This comprehensive characterization not only confirms the successful synthesis of NVO_d with specific morphological traits but also underscores the homogeneity of elemental distribution, which is crucial for the consistent electrochemical performance of these materials in AZIBs.

Furthermore, transmission electron microscopy (TEM) analysis was conducted to ascertain the morphology of the NVO_d system. The outcomes of this TEM analysis are depicted in Figure 4. As illustrated in Figure 4, the TEM results unambiguously confirmed the presence of a nanosheet structure, which is in alignment with the SEM findings. This congruence between TEM and SEM analyses reinforces the accuracy of our morphological characterization of the material.

The comprehensive X-ray photoelectron spectroscopy (XPS) analysis depicted in Figure 5a confirms the presence of V, O, N, and carbon (C) elements in both NVO and NVO_d samples, with S elements conspicuously absent, as demonstrated in Figure 5b. This observation aligns with the findings obtained from EDS mapping analysis, further corroborating the purity of the synthesized materials. Figure 5c showcases the XPS spectra of the V 2p for both NVO and NVO_d-3 samples. The incorporation of oxygen O_d is evidenced by a valence state transition of vanadium, with a partial reduction from V^{5+} to V^{4+}. This transition is attributed to the reduction in the number of neighboring oxygen atoms surrounding the vanadium atoms, leading to an increased electron density in the vicinity of V. Such a phenomenon is indicative of the structural modifications within the VO framework prompted by the integration of O_ds, which not only facilitates the embedding and de-embedding processes of Zn^{2+} ions but also contributes additional electrons, thereby augmenting the material's capacity.
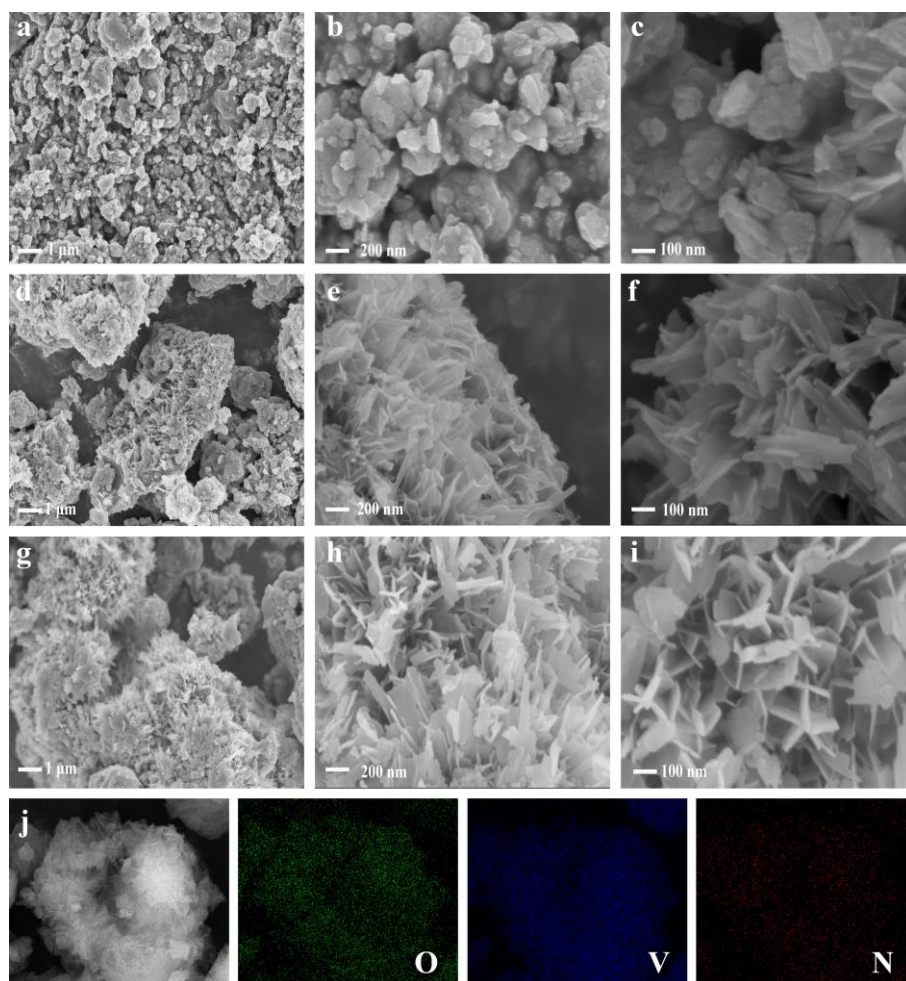
Figure 3. SEM images of (**a–c**) NVO_d-2, (**d–f**) NVO_d-3, and (**g–i**) NVO_d-4 at different resolutions; (**j**) EDS mapping elemental analysis of NVO_d-3.
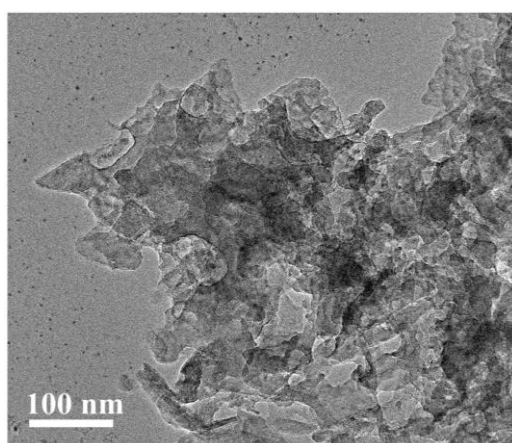

Figure 4. TEM image of NVO_d-3.

Further elucidating the structural and compositional nuances, Figure 5d presents the XPS spectra of the O 1s for both NVO and NVO_d-3. The peak associated with lattice oxygen (V-O) in NVO is recorded at 530.18 eV. In contrast, for NVO_d-3, this peak shifts slightly to 530.28 eV, with the peak indicative of O_d observed at 531.28 eV. This subtle shift not only confirms the successful introduction of O_ds but also highlights the resultant

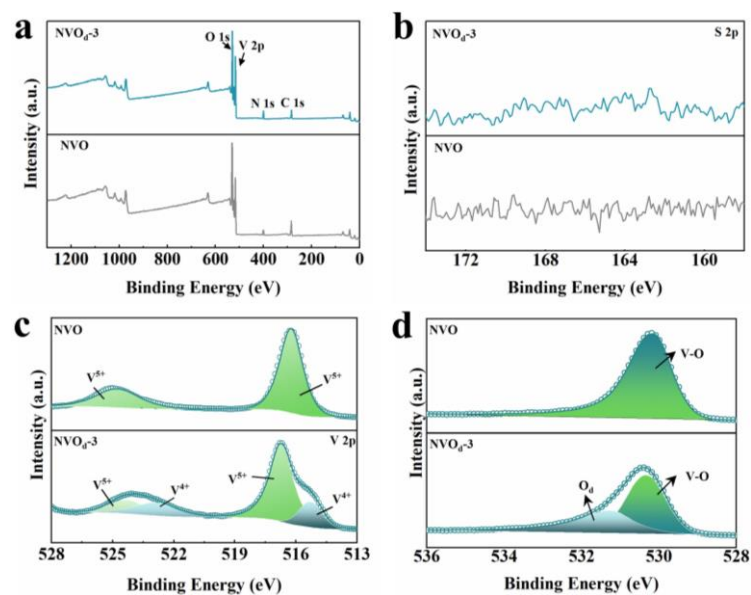structural rearrangement and its implications on the electronic environment surrounding the V centers.

Figure 5. (**a**) XPS survey of NVO_d-3 and NVO; (**b**) S 2p XPS spectra of NVO_d-3 and NVO; (**c**) V 2p XPS spectra of NVO_d-3 and NVO; (**d**) O 1s XPS spectra of NVO_d-3 and NVO.

2.3. Electrochemical Properties Characterization

O_ds can serve as pivotal contributors to the charge transfer process, offering numerous jump sites and active sites that are instrumental in defining the structural stability of cathode materials. To evaluate the influence of O_ds on electrochemical performance, a zinc//NVO_d battery was constructed, utilizing zinc foil as the anode and 3 M $Zn(CF_3SO_3)_2$ as the electrolyte. The electrochemical properties of this assembly were subsequently investigated to ascertain the impact of O_ds on the battery's performance metrics.

Figure 6a illustrates the specific capacities of the electrode materials NVO_d-2, NVO_d-3, NVO_d-4, and NVO, evaluated at a current density of 0.2 A g^{-1}. It is observed that an increase in O_d content correlates with enhancements in both the specific capacity and cycling stability of the electrodes. However, this trend reverses when the O_d content surpasses a certain threshold, leading to a reduction in electrode capacity. This decline in performance, particularly noted for NVO_d-4 which demonstrated a capacity of 386 mAh g^{-1} at 0.2 A g^{-1}, can be attributed to structural degradation resulting from an overabundance of O_ds, underscoring the critical balance required in optimizing O_d levels for improved electrochemical performance.

The investigation into the electrochemical behavior of NVO_d materials enriched with O_ds reveals a superior performance compared to pristine NVO materials. This enhancement suggests that O_ds play a vital role in augmenting the electrochemical attributes of ammonium vanadate-based cathodes. Specifically, the NVO_d-3 cathode distinguishes itself by delivering an exceptional initial discharge capacity of over 458.3 mAh g^{-1} at a current density of 0.2 A g^{-1}. This capacity significantly surpasses those of several previously reported AZIB cathodes, including VO_2 (357 mAh g^{-1}) [32], $Na_{0.33}V_2O_5$ (367.1 mAh g^{-1}) [33], $Zn_2(OH)VO_4$ (204 mAh g^{-1}) [34], and other ammonium vanadate variants such as $(NH_4)_2V_4O_9$ (378 mAh g^{-1}) [35] and $(NH_4)_2V_6O_{16}$ (323.5 mAh g^{-1}) [36]. Remarkably, after 15 cycles, the NVO_d-3 cathode achieved a peak discharge capacity of 479.3 mAh g^{-1}. Moreover, after enduring 50 cycles, it maintained a capacity retention rate of approximately 90.1%, underscoring its exceptional durability and performance consistency in AZIB applications.
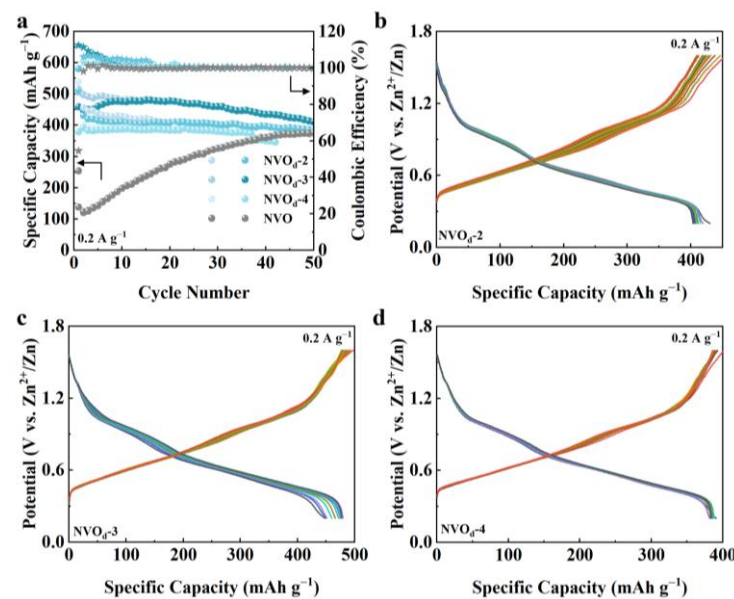
Figure 6. (**a**) Cycling performance of NVO_d-2, NVO_d-3, NVO_d-4, and NVO at 0.2 A g^{-1}; galvanostatic charge–discharge profiles of (**b**) NVO_d-2, (**c**) NVO_d-3, and (**d**) NVO_d-4 for the first 20 cycles, correlating with the cycling performance presented in (**a**). The active material loading is 1 mg cm^{-2}.

Figure 6b–d present the galvanostatic charge–discharge profiles of NVO_d-2, NVO_d-3, and NVO_d-4, each tested at a current density of 0.2 A g^{-1}. Notably, all profiles feature two distinct, relatively flat charge–discharge plateaus, indicative of the complex electrochemical processes underway. These plateaus are attributed to the sequential reactions occurring within the NVO_d electrode during the charge–discharge cycle, specifically the embedding and de-embedding of Zn^{2+} ions coupled with the electron redox reactions.

Moreover, subsequent to the initial cycle, the profiles of these curves and their associated charge–discharge plateaus exhibit remarkable consistency across subsequent cycles, demonstrating a high degree of reproducibility with minimal deviation. Among the variants, NVO_d-4 exhibits the most pronounced curve overlap, albeit with the lowest discharge capacity. Conversely, NVO_d-2, while showing less pronounced curve overlap, achieves a slightly higher capacity than NVO_d-4. NVO_d-3 stands out by offering an optimal balance of high capacity and stability, showcasing its efficacy in maintaining performance across cycles. This observation underscores the critical interplay between structural integrity and electrochemical functionality within the NVO_d materials, highlighting the nuanced impact of O_d concentration on the overall performance of ammonium vanadate cathodes.

Figure 7a delineates the rate capabilities of NVO_d-2, NVO_d-3, and NVO_d-4 across a current density range from 0.1 to 10 A g^{-1}, while Figure 7b details the rate performance of pristine NVO within the same current density spectrum. Comparative analysis of the data presented in these figures reveals that NVO_d variants manifest a significantly enhanced rate performance in comparison to pristine NVO. Notably, NVO_d-3 demonstrates remarkable capacities at varying current densities, achieving 476.4, 461.2, 427.8, 400.2, 340.8, 274.1, 188.7, and 148.7 mAh g^{-1} at current densities of 0.1, 0.2, 0.5, 1, 3, 5, 8, and 10 A g^{-1}, respectively. In contrast, NVO exhibits capacities of 299.7, 294.4, 281.5, 250.4, 96.2, and 13.8 mAh g^{-1} at 0.1, 0.2, 0.5, 1, 3, and 5 A g^{-1}, respectively, indicating a pronounced disparity in performance.

Both NVO_d-2 and NVO_d-4 display reversible specific capacities that are lower than those of NVO_d-3 at all tested current densities. Specifically, NVO_d-2 presents capacities of 449.3, 441.4, 420.1, 377.4, 233.2, 109.4, 38.1, and 12.3 mAh g^{-1}, while NVO_d-4 exhibits capacities of 449.1, 440.3, 420.1, 400.2, 343.3, 275.4, 165.4, and 101.3 mAh g^{-1} at 0.1, 0.2, 0.5, 1, 3, 5, 8, and 10 A g^{-1}, respectively. Upon reverting the current density back to 0.1 A g^{-1}, all three materials demonstrate the ability to recover to their initial capacity values. Remarkably, the Zn//NVO_d-3 battery sustains a high capacity of 465.2 mAh g^{-1} upon this return

to the baseline current density, significantly outstripping the Zn//NVO, which registers a capacity of 304.2 mAh g^{-1}. The superior rate capability of NVO$_d$-3 underscores the beneficial impact of strategically introduced defects, which evidently enhance the kinetics of Zn^{2+} embedding and de-embedding.
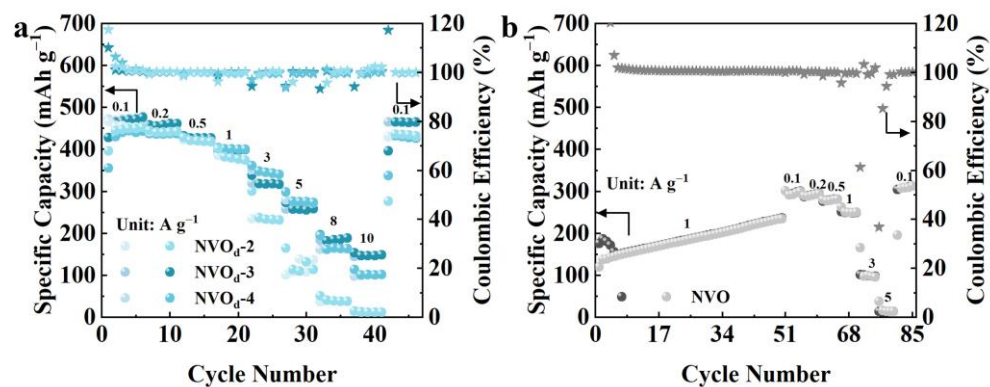

Figure 7. Rate performance of (**a**) NVO$_d$-2, NVO$_d$-3, NVO$_d$-4, and (**b**) NVO. The active material loading is 1 mg cm^{-2}.

Furthermore, the long-term cycling performance of NVO$_d$-2, NVO$_d$-3, NVO$_d$-4, and pristine NVO was assessed, with the findings presented in Figure 8. These evaluations were conducted at a rigorous current density of 10 A g^{-1} to test the endurance of the materials under high-rate conditions. Notably, NVO$_d$-3 initiated the test with an initial capacity of 198 mAh g^{-1}. This capacity observed a decrement during the initial cycles but reached a stable capacity of 169 mAh g^{-1} after the first 10 cycles. Impressively, after 1500 cycles, NVO$_d$-3 maintained a capacity retention of 65.4% relative to its stabilized capacity, highlighting its durability and resilience over extended cycling.
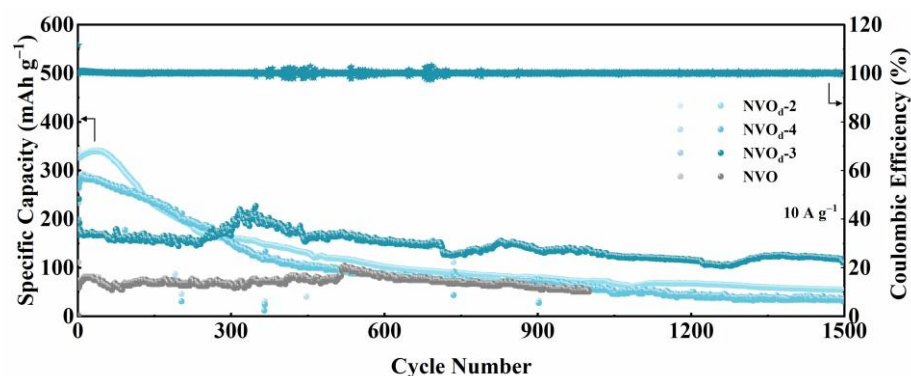

Figure 8. Cycling performance of NVO$_d$-2, NVO$_d$-3, NVO$_d$-4, and NVO at 10 A g^{-1}. The active material loading is 1 mg cm^{-2}.

In contrast, pristine NVO started with an initial capacity of less than 100 mAh g^{-1}, underlining a significant disparity in performance when compared to the NVO$_d$ variants. While both NVO$_d$-2 and NVO$_d$-4 exhibited promising initial capacities exceeding 250 mAh g^{-1}, they suffered a precipitous decline to merely 30% of their initial capacities after 400 cycles, highlighting challenges in maintaining long-term stability. Among the materials tested, NVO$_d$-3 distinguished itself by demonstrating a commendable balance of high reversible specific capacity and sustained cycle stability.

To further investigate the electrochemical reaction mechanisms underpinning its performance, cyclic voltammetry (CV) tests were executed using an electrochemical workstation across a voltage window of 0.2 to 1.6 V, employing scan rates of 0.1, 0.2, 0.4, 0.6, and 0.8 mV s^{-1}, as depicted in Figure 9a,d,g. The CV results elucidate that an increase in the scan rate leads to enhanced polarization, which in turn precipitates a discernible

shift in the oxidation and reduction peaks. Specifically, the oxidation peaks are observed to migrate towards higher voltages, while the reduction peaks shift towards lower voltages, indicating kinetic limitations within the electrochemical processes. Despite these shifts, the overall morphology of the CV curves remains consistent across the various scan rates.
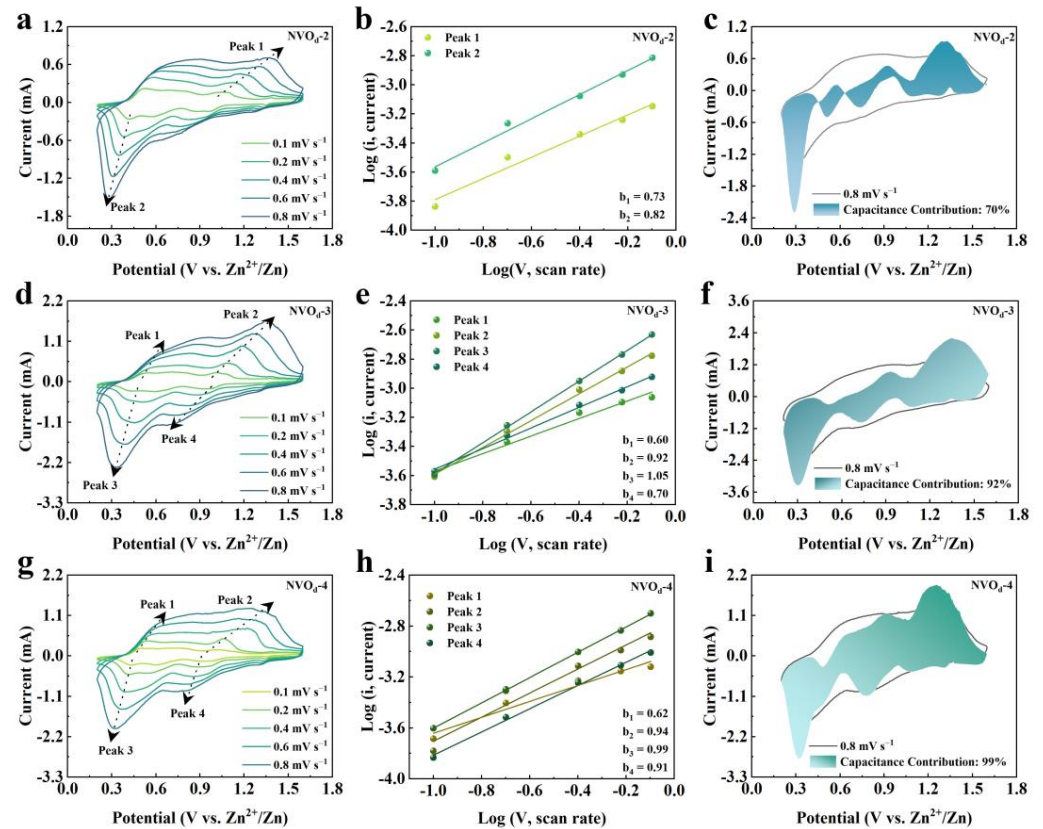

Figure 9. CV curves of electrode at different scan rates (**a**) NVO_d-2, (**d**) NVO_d-3, and (**g**) NVO_d-4; the linear relationship between peak currents log(i) and the square root of scan rates log(v) (**b**) NVO_d-2, (**e**) NVO_d-3, and (**h**) NVO_d-4; pseudocapacitance contribution at 0.8 mV s^{-1} (**c**) NVOd-2, (**f**) NVO_d-3, and (**i**) NVO_d-4. The active material loading is 1 mg cm^{-2}.

The peak current density (i) and the scan rate (v) are governed by the following formulas, used to quantify the influence of capacitance and diffusion control on the overall capacitance:

$$i = av^b \tag{1}$$

$$\log(i) = \log(a) + b\log(v) \tag{2}$$

$$i = k_1 v + k_2 v^{1/2} \tag{3}$$

where the value of b reflects the degree to which the electrochemical reaction is controlled by diffusion or capacitance. Generally, when b approaches 0.5, it indicates a typical diffusion-controlled process, and when b approaches 1, it suggests pseudocapacitive-dominated behavior. As shown in Figure 9b,e,h, the characteristic peak b values for NVO_d-2, NVO_d-3, and NVO_d-4 lie between 0.5 and 1, indicating contributions from both mechanisms, with pseudocapacitance playing a dominant role. Some peak values are largely influenced by capacitive control, approaching 1.

As delineated in Figure 9c,f,i, the analysis of pseudocapacitive contributions for NVO_d-2, NVO_d-3, and NVO_d-4 at a scan rate of 0.8 mV s^{-1} reveals contribution rates of 70%, 92%, and 99%, respectively. Furthermore, Figure 10a,c,e highlight the variation in pseudocapacitive contribution rates of NVO_d-2, NVO_d-3, and NVO_d-4 across scan rates ranging from 0.1 to 0.8 mV s^{-1}. For NVO_d-2, the capacitive contribution escalates from

41% to 70%, for NVO$_d$-3, it increases from 79% to 92%, and for NVO$_d$-4, it advances from 91% to 99%. These observations underscore a distinct trend: with an increment in the concentration of oxygen defects, there is a corresponding increase in the pseudocapacitive contribution rate of the material.
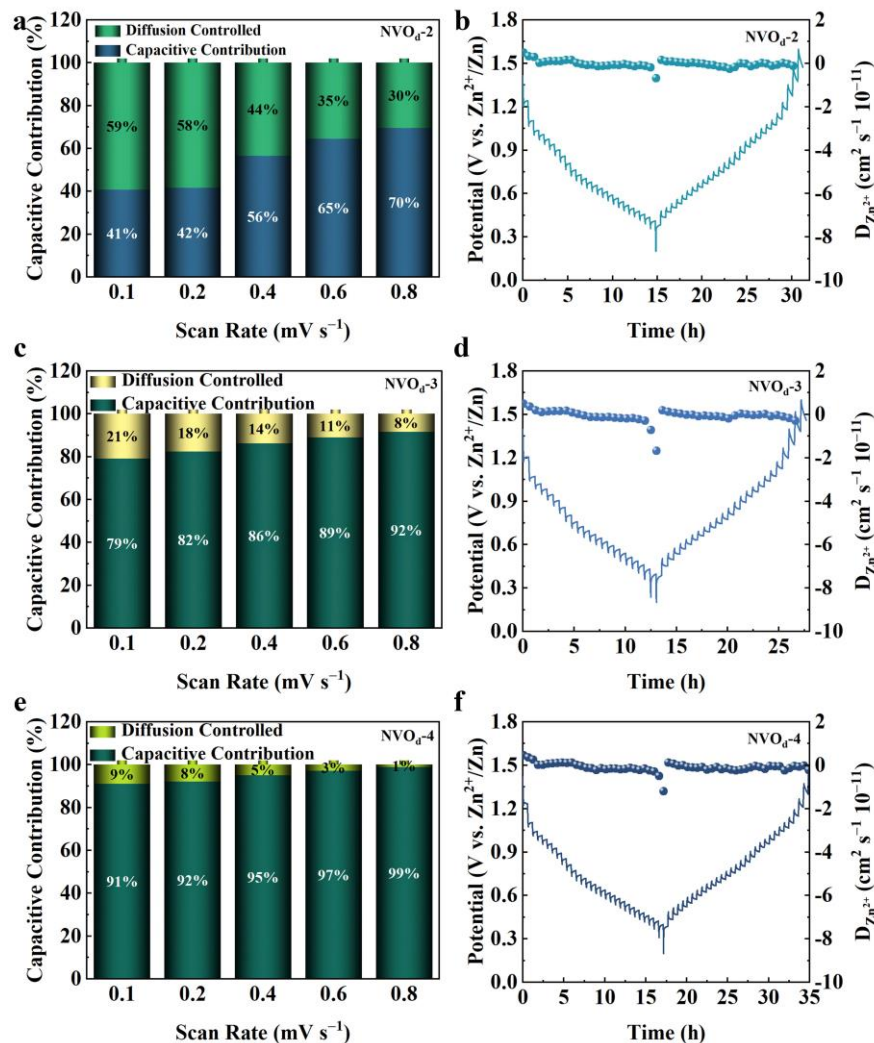

Figure 10. Capacitance contribution diagram at different scan rates (**a**) NVO$_d$-2, (**c**) NVO$_d$-3, and (**e**) NVO$_d$-4; GITT diagram of (**b**) NVO$_d$-2, (**d**) NVO$_d$-3, and (**f**) NVO$_d$-4. The active material loading is 1 mg cm^{-2}.

The employment of the galvanostatic intermittent titration technique (GITT) provided further insight into the dynamics of Zn^{2+} diffusion and its contribution to charge transfer within the material. The GITT experiments were performed at a controlled current density of 0.2 A g^{-1}, incorporating a relaxation period of 30 min and a data acquisition interval of 10 s. As illustrated in Figure 10b,d,f, the derived diffusion coefficients for Zn^{2+} across the examined materials were found to range between 10^{-10} and 10^{-11} cm^2 s^{-1}, indicating a moderate diffusion rate conducive to electrochemical activity. Notably, the diffusion coefficient for NVO$_d$-3 was marginally superior compared to those of NVO$_d$-2 and NVO$_d$-4.

Finally, to understand the implications of electrochemical cycling on the morphological evolution of electrodes, we conducted an examination of the morphological changes using SEM. This analysis was focused on cathode samples in various states: pristine (uncycled), fully discharged to 0.2 V, and fully charged to 1.6 V. The findings, depicted in Figure 11, provide a visual representation of the dynamic changes occurring at the electrode surface throughout the cycling process.
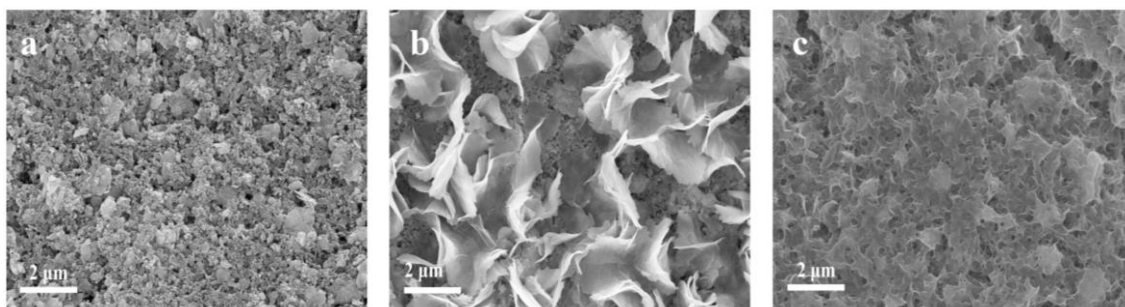
Figure 11. SEM diagram of the positive pole piece in different charging and discharging states: (**a**) initial state, (**b**) discharged to 0.2 V, and (**c**) charged to 1.6 V. The active material loading is 1 mg cm^{-2}.

Initially, SEM images of the pristine electrodes illustrated a clean surface, indicating a uniform and defect-free material. Upon discharging to 0.2 V, a distinct morphological transformation was observed. The electrode surfaces developed micrometer-scale flakes, indicative of the active material's response to the electrochemical environment. These features were attributed to the accommodation of Zn^{2+} ions within the electrode matrix, leading to the creation of new surface structures.

Remarkably, when the electrodes were fully charged to 1.6 V, the micrometer-scale flakes disappeared, reverting the surface to a state closely resembling the initial pristine condition. This reversible morphological change is a testament to the electrode's ability to undergo significant transformations while maintaining structural integrity and functionality. The disappearance of the flakes upon recharging demonstrates the excellent reversibility of Zn^{2+} intercalation/de-intercalation and the resilience of the electrode material under cycling conditions.

3. Materials and Methods

3.1. Calculation Method

The DFT calculations were executed utilizing the Vienna Ab Initio Simulation Package (VASP) [37]. The Perdew–Burke–Ernzerhof (PBE) functional was employed to encapsulate the exchange–correlation interactions [38]. The computational approach incorporated a plane-wave basis set with an energy cutoff of 400 eV, paired with the Projector Augmented Wave (PAW) method [39,40]. Convergence thresholds for the self-consistent iterations and forces were set at 1×10^{-5} eV and 0.01 eV Å^{-1}, respectively. The Brillouin zone was sampled using a $4 \times 2 \times 1$ Γ-centered k-point mesh for the relaxation of the geometric structure and total energy calculations. For a more granular calculation of the density of states, an enhanced $8 \times 8 \times 1$ Γ-centered k-mesh was employed.

3.2. Preparation of Material

The synthesis of oxygen-deficient $(NH_4)_2V_{10}O_{25} \cdot 8H_2O$ nanoplates was achieved through a one-step water bath method. Initially, 0.468 g (4 mmol) of commercial NH$_4$VO$_3$ powder was solubilized in 50 mL of deionized water within a water bath maintained at 70 °C. The solution transitioned to a pale yellow hue upon complete dissolution of the reactant. To this solution, thiourea, in varying molar quantities (2, 3, 4 mmol), was introduced under continuous agitation. The solution's pH was then carefully adjusted to approximately 2 by the dropwise addition of 0.1 M dilute hydrochloric acid, followed by a stirring period of 30 min. The reaction was subsequently extended for an additional 2 h under a 90 °C oil bath, culminating in the formation of a dark green suspension. Following a natural cooling process to ambient temperature, the resultant product was isolated, purified with deionized water and ethanol, and desiccated in a vacuum oven at 60 °C, over a 24 h period, yielding the final nanoplate structures. Depending on the molar amount of thiourea utilized, the resultant nanoplates were designated as NVOd-2 (2 mmol thiourea),

NVOd-3 (3 mmol thiourea), and NVOd-4 (4 mmol thiourea). For comparative purposes, a control sample of NVO material was synthesized under identical conditions, albeit in the absence of thiourea.

3.3. Electrode Fabrication

The fabrication of the electrodes commenced with the thorough mixing of the active material, acetylene black, and polyvinylidene fluoride (PVDF) in a 6:3:1 mass ratio, under ambient conditions. This mixture was ground until a homogenous consistency was achieved. Subsequently, N-Methyl-2-pyrrolidone (NMP) was incrementally introduced to the blend, with continuous grinding and stirring, until the slurry attained a uniform consistency and displayed an oily black luster.

This resultant slurry was meticulously coated onto a 0.3 mm thick titanium foil, serving as the current collector. The coated foil was then allowed to rest for a designated period before being subjected to a drying process in a vacuum oven, maintained at 110 °C for 12 h. Following this, the dried, coated foil was processed using a pellet press to yield circular discs, each with a diameter of 1 cm. This process ensured an active material loading on the titanium foil of approximately 1 mg cm^{-2}.

3.4. Structure and Morphology Characterization

The crystalline structures and phase compositions of the synthesized materials were meticulously analyzed using XRD techniques. These analyses were conducted utilizing a Smart Lab SE diffractometer, which is equipped with Cu Kα radiation (λ = 1.5418 Å), across a 2θ range from 5° to 80°. This broad range allows for a comprehensive identification of crystalline phases present in the samples.

To further investigate the chemical states and elemental valence changes within the materials, XPS measurements were performed. These analyses were carried out using a Thermo ESCALAB 250Xi instrument (Waltham, MA, USA), which is renowned for its precision in determining the chemical composition and electronic state of elements within materials.

The surface morphology, internal crystallography, and elemental dispersion across the samples were elucidated through field emission SEM. For these examinations, a Hitachi SU8010 microscope (Tokyo, Japan) was utilized under standard ambient conditions, providing high-resolution images that revealed the detailed structural and morphological features of the materials.

Additionally, the presence of O_d in the materials was confirmed through EPR spectroscopy. These measurements were conducted using an EMX nano spectrometer, which is specifically designed for the detection of unpaired electrons, providing indirect evidence of the oxygen vacancies within the crystal lattice of the synthesized nanoplates.

3.5. Electrochemical Measurements

The electrochemical properties of the synthesized materials were thoroughly evaluated through the assembly and testing of CR2032-type button cells, which served as the prototype electrochemical cells for this investigation. In the assembly process, zinc foil was utilized as the anode material, while titanium foil acted as the current collector. Filter paper was chosen for its role as the separator, ensuring physical separation and electrolyte permeability between the anode and cathode materials. The entire cell assembly was performed in an electrolyte solution composed of 3M zinc trifluoromethanesulfonate ($Zn(CF_3SO_3)_2$), under standard laboratory conditions at ambient temperature.

For the purpose of electrochemical characterization, CV and EIS analyses were conducted using a CHI 760E electrochemical workstation. These measurements were carried out within a predefined voltage window of 0.2 to 1.6 V, aimed at understanding the redox behavior and electrochemical kinetics of the cells.

Additionally, the performance of the assembled cells, including their charge–discharge capabilities and cycling stability, was meticulously evaluated using a LAND battery testing

system. This system facilitated the detailed assessment of the electrochemical behavior under various operating conditions, providing valuable insights into the potential applicability of the materials for energy storage purposes.

4. Conclusions

Guided by theoretical calculations, we have rationally designed NVO_d nanosheets as a cathode material for aqueous AZIBs, which exhibit superior capacity and excellent cyclic performance. The genesis of the O_ds can be traced back to the incorporation of thiourea during the synthesis process. These O_ds play a pivotal role in modulating the internal structure of NVO_d, enhancing its conductivity, and thereby augmenting the electrochemical kinetics. Such improvements culminate in enhanced cyclic performance. Exploiting these attributes, the NVO_d-3 electrode we prepared demonstrated a remarkable capacity of 408 mAh g^{-1} at a current density of 0.1 A g^{-1}, alongside outstanding stability across 1500 cycles with a capacity retention of 70.4%. Moreover, our findings reveal that the concentration of O_d critically influences the pseudocapacitive contribution of the material. Specifically, the variant with the highest concentration of oxygen vacancies, NVO_d-4, showcases a pseudocapacitive contribution rate of 91% at a scan rate of 0.1 mV s^{-1}. These results underscore the significance of O_ds in the development of high-performance layered cathode materials for energy storage applications.

Author Contributions: Conceptualization, H.L. and X.C.; methodology, H.L. and Y.Z.; software, Y.Z.; validation, H.L., X.C. and Y.Z.; formal analysis, H.L. and X.C.; investigation, H.L., X.C. and Y.Z.; resources, X.C.; data curation, Y.Z.; writing—original draft preparation, H.L.; writing—review and editing, H.L., X.C. and Y.Z.; visualization, X.C. and Y.Z.; supervision, H.L.; project administration, H.L.; funding acquisition, H.L. All authors have read and agreed to the published version of the manuscript.

Data Availability Statement: The data presented in this study are available on request from the corresponding author.

Conflicts of Interest: The authors declare no conflicts of interest.

References

1. Jia, X.; Liu, C.; Neale, Z.G.; Yang, J.; Cao, G. Active materials for aqueous zinc ion batteries: Synthesis, crystal structure, morphology, and electrochemistry. *Chem. Rev.* **2020**, *120*, 7795–7866. [CrossRef] [PubMed]
2. Zheng, Y.; Yao, Y.; Ou, J.; Li, M.; Luo, D.; Dou, H.; Li, Z.; Amine, K.; Yu, A.; Chen, Z. A review of composite solid-state electrolytes for lithium batteries: Fundamentals, key materials and advanced structures. *Chem. Soc. Rev.* **2020**, *49*, 8790–8839. [CrossRef] [PubMed]
3. Lin, X.; Khosravinia, K.; Hu, X.; Li, J.; Lu, W. Lithium plating mechanism, detection, and mitigation in lithium-ion batteries. *Prog. Energy Combust. Sci.* **2021**, *87*, 100953. [CrossRef]
4. Shadike, Z.; Tan, S.; Wang, Q.-C.; Lin, R.; Hu, E.; Qu, D.; Yang, X.-Q. Review on organosulfur materials for rechargeable lithium batteries. *Mater. Horiz.* **2021**, *8*, 471–500. [CrossRef] [PubMed]
5. Selvakumaran, D.; Pan, A.; Liang, S.; Cao, G. A review on recent developments and challenges of cathode materials for rechargeable aqueous Zn-ion batteries. *J. Mater. Chem. A* **2019**, *7*, 18209–18236. [CrossRef]
6. Zhang, N.; Wang, J.-C.; Guo, Y.-F.; Wang, P.-F.; Zhu, Y.-R.; Yi, T.-F. Insights on rational design and energy storage mechanism of Mn-based cathode materials towards high performance aqueous zinc-ion batteries. *Coord. Chem. Rev.* **2023**, *479*, 215009. [CrossRef]
7. Alfaruqi, M.H.; Mathew, V.; Gim, J.; Kim, S.; Song, J.; Baboo, J.P.; Choi, S.H.; Kim, J. Electrochemically induced structural transformation in a γ-MnO$_2$ cathode of a high capacity zinc-ion battery system. *Chem. Mater.* **2015**, *27*, 3609–3620. [CrossRef]
8. Chen, D.; Lu, M.; Cai, D.; Yang, H.; Han, W. Recent advances in energy storage mechanism of aqueous zinc-ion batteries. *J. Energy Chem.* **2021**, *54*, 712–726. [CrossRef]

9.   Wu, J.; Chi, X.; Liu, Y.; Yang, J.; Liu, Y. Electrochemical characterization of hollow urchin-like MnO_2 as high-performance cathode for aqueous zinc ion batteries. *J. Electroanal. Chem.* **2020**, *871*, 114242. [CrossRef]

10. Mathew, V.; Sambandam, B.; Kim, S.; Kim, S.; Park, S.; Lee, S.; Alfaruqi, M.H.; Soundharrajan, V.; Islam, S.; Putro, D.Y.; et al. Manganese and vanadium oxide cathodes for aqueous rechargeable zinc-ion batteries: A focused view on performance, mechanism, and developments. *ACS Energy Lett.* **2020**, *5*, 2376–2400. [CrossRef]

11. Sun, W.; Wang, F.; Hou, S.; Yang, C.; Fan, X.; Ma, Z.; Gao, T.; Han, F.; Hu, R.; Zhu, M.; et al. Zn/MnO_2 battery chemistry with H^+ and Zn^{2+} coinsertion. *J. Am. Chem. Soc.* **2017**, *139*, 9775–9778. [CrossRef] [PubMed]

12. Yan, M.; He, P.; Chen, Y.; Wang, S.; Wei, Q.; Zhao, K.; Xu, X.; An, Q.; Shuang, Y.; Shao, Y.; et al. Water-lubricated intercalation in $V_2O_5 \cdot nH_2O$ for high-capacity and high-rate aqueous rechargeable zinc batteries. *Adv. Mater.* **2018**, *30*, 1703725. [CrossRef] [PubMed]

13. Chen, D.; Lu, M.; Wang, B.; Cheng, H.; Yang, H.; Cai, D.; Han, W.; Fan, H.J. High-mass loading $V_3O_7 \cdot H_2O$ nanoarray for Zn-ion battery: New synthesis and two-stage ion intercalation chemistry. *Nano Energy* **2021**, *83*, 105835. [CrossRef]

14. Zhang, N.; Dong, Y.; Jia, M.; Bian, X.; Wang, Y.; Qiu, M.; Xu, J.; Liu, Y.; Jiao, L.; Cheng, F. Rechargeable aqueous $Zn-V_2O_5$ battery with high energy density and long cycle life. *ACS Energy Lett.* **2018**, *3*, 1366–1372. [CrossRef]

15. Zhang, N.; Jia, M.; Dong, Y.; Wang, Y.; Xu, J.; Liu, Y.; Jiao, L.; Cheng, F. Hydrated layered vanadium oxide as a highly reversible cathode for rechargeable aqueous zinc batteries. *Adv. Funct. Mater.* **2019**, *29*, 1807331. [CrossRef]

16. Zampardi, G.; Mantia, F.L. Prussian blue analogues as aqueous Zn-ion batteries electrodes: Current challenges and future perspectives. *Curr. Opin. Electrochem.* **2020**, *21*, 84–92. [CrossRef]

17. Zhou, T.; Zhu, L.; Xie, L.; Han, Q.; Yang, X.; Chen, L.; Wang, G.; Cao, X. Cathode materials for aqueous zinc-ion batteries: A mini review. *J. Colloid. Interf. Sci.* **2022**, *605*, 828–850. [CrossRef] [PubMed]

18. Zhang, L.; Chen, L.; Zhou, X.; Liu, Z. Towards high-voltage aqueous metal-ion batteries beyond 1.5 V: The zinc/zinc hexacyanoferrate system. *Adv. Energy Mater.* **2015**, *5*, 1400930. [CrossRef]

19. Wu, X.; Qi, Y.; Hong, J.J.; Li, Z.; Hernandez, A.S.; Ji, X. Rocking-chair ammonium-ion battery: A highly reversible aqueous energy storage system. *Angew. Chem. Int. Ed.* **2017**, *56*, 13026–13030. [CrossRef]

20. Konarov, A.; Voronina, N.; Jo, J.H.; Bakenov, Z.; Sun, Y.-K.; Myung, S.-T. Present and future perspective on electrode materials for rechargeable zinc-ion batteries. *ACS Energy Lett.* **2018**, *3*, 2620–2640. [CrossRef]

21. Kim, J.; Kim, J.H.; Ariga, K. Redox-active polymers for energy storage nanoarchitectonics. *Joule* **2017**, *1*, 739–768. [CrossRef]

22. Kundu, D.; Oberholzer, P.; Glaros, C.; Bouzid, A.; Tervoort, E.; Pasquarello, A.; Niederberger, M. Organic cathode for aqueous Zn-ion batteries: Taming a unique phase evolution toward stable electrochemical cycling. *Chem. Mater.* **2018**, *30*, 3874–3881. [CrossRef]

23. Cui, H.; Ma, L.; Huang, Z.; Chen, Z.; Zhi, C. Organic materials-based cathode for zinc ion battery. *SmartMat* **2022**, *3*, 565–581. [CrossRef]

24. Deng, Y.-P.; Liang, R.; Jiang, G.; Jiang, Y.; Yu, A.; Chen, Z. The current state of aqueous Zn-based rechargeable batteries. *ACS Energy Lett.* **2020**, *5*, 1665–1675. [CrossRef]

25. Wang, Z.; Zhang, Y.; Ye, H.; Cheng, H.; Cai, X.; Wei, M.; Gu, Y.; Liu, C.; Pan, Y.; Jia, D.; et al. From theory to practice: Optimizing Mg^{2+} ratios in spinel MgV_2O_4 for elevated performance cathode in aqueous zinc-ion batteries. *J. Energy Storage* **2024**, *83*, 110622. [CrossRef]

26. Cheng, H.; Zhang, Y.; Cai, X.; Liu, C.; Wang, Z.; Ye, H.; Pan, Y.; Jia, D.; Lin, H. Boosting zinc storage performance of Li_3VO_4 cathode material for aqueous zinc ion batteries via carbon-incorporation: A study combining theory and experiment. *Small* **2024**, *20*, 2305762. [CrossRef] [PubMed]

27. Liu, Y.; Liu, Y.; Wu, X. Defect engineering of vanadium-based electrode materials for zinc ion battery. *Chin. Chem. Lett.* **2023**, *34*, 107839. [CrossRef]

28. Lai, J.; Tang, H.; Zhu, X.; Wang, Y. A hydrated $NH_4V_3O_8$ nanobelt electrode for superior aqueous and quasi-solid-state zinc ion batteries. *J. Mater. Chem. A* **2019**, *7*, 23140–23148. [CrossRef]

29. Wang, X.; Xi, B.; Feng, Z.; Chen, W.; Li, H.; Jia, Y.; Feng, J.; Qian, Y.; Xiong, S. Layered $(NH_4)_2V_6O_{16} \cdot 1.5H_2O$ nanobelts as a high-performance cathode for aqueous zinc-ion batteries. *J. Mater. Chem. A* **2019**, *7*, 19130–19139. [CrossRef]

30. Liu, C.; Zhang, Y.; Cheng, H.; Cai, X.; Jia, D.; Lin, H. "Dual-engineering" strategy to regulate $NH_4V_4O_{10}$ as cathodes for high-performance aqueous zinc ion batteries. *Small* **2023**, *19*, 2301870. [CrossRef]

31. Bao, M.; Zhang, Z.; An, X.; Liu, J.; Feng, J.; Xi, B.; Xiong, S. Introducing Ce ions and oxygen defects into V_2O_5 nanoribbons for efficient aqueous zinc ion storage. *Nano Res.* **2023**, *16*, 2445–2453. [CrossRef]

32. Liu, N.; Wu, X.; Yin, Y.; Chen, A.; Zhao, C.; Guo, Z.; Fan, L.; Zhang, N. Constructing the efficient ion diffusion pathway by introducing oxygen defects in Mn_2O_3 for high-performance aqueous zinc-ion batteries. *ACS Appl. Mater. Interfaces* **2020**, *12*, 28199–28205. [CrossRef]

33. Ding, J.; Du, Z.; Gu, L.; Li, B.; Wang, L.; Wang, S.; Gong, Y.; Yang, S. Ultrafast Zn^{2+} intercalation and deintercalation in vanadium dioxide. *Adv. Mater.* **2018**, *30*, 1800762. [CrossRef]

34. Kundu, D.; Adams, B.D.; Duffort, V.; Vajargah, S.H.; Nazar, L.F. A high-capacity and long-life aqueous rechargeable zinc battery using a metal oxide intercalation cathode. *Nat. Energy* **2016**, *1*, 16119. [CrossRef]

35. Zhang, Y.; Jiang, H.; Xu, L.; Gao, Z.; Meng, C. Ammonium vanadium oxide [$(NH_4)_2V_4O_9$] sheets for high capacity electrodes in aqueous zinc ion batteries. *ACS Appl. Energy Mater.* **2019**, *2*, 7861–7869. [CrossRef]

36. Xu, L.; Zhang, Y.; Jiang, H.; Zheng, J.; Dong, X.; Hu, T.; Meng, C. Facile hydrothermal synthesis and electrochemical properties of $(NH_4)_2V_6O_{16}$ nanobelts for aqueous rechargeable zinc ion batteries. *Colloids Surf. A* **2020**, *593*, 124621. [CrossRef]

37. Kresse, G.; Furthmüller, J. Efficient iterative schemes for ab initio total-energy calculations using a plane-wave basis set. *Phys. Rev. B* **1996**, *54*, 11169–11186. [CrossRef]

38. Perdew, J.P.; Burke, K.; Ernzerhof, M. Generalized gradient approximation made simple. *Phys. Rev. Lett.* **1996**, *77*, 3865–3868. [CrossRef] [PubMed]

39. Kresse, G.; Joubert, D. From ultrasoft pseudopotentials to the projector augmented-wave method. *Phys. Rev. B* **1999**, *59*, 1758–1775. [CrossRef]

40. Blöchl, P.E. Projector augmented-wave method. *Phys. Rev. B* **1994**, *50*, 17953–17979. [CrossRef]